Minerals Engineering 203 (2023) 108318

Contents lists available at ScienceDirect

Minerals Engineering

journal homepage: www.elsevier.com/locate/mineng

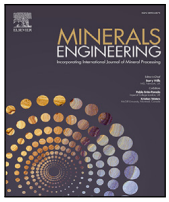

Numerical modelling of microwave irradiated rock fracture

Martina Pressacco [a,*], Jari J.J. Kangas [b], Timo Saksala [a]

[a] Tampere University, Faculty of Built Environment, Tampere, 33720, Finland
[b] Tampere University, Faculty of Information Technology and Communication Sciences, Tampere, 33720, Finland

ARTICLE INFO

Keywords:
Rock fracturing
Microwave irradiation
Finite Element Method
Compressive strength
Numerical simulations

ABSTRACT

Rock fracturing through microwave irradiation has received significant attention recently as a viable pretreatment for improving the energy efficiency of comminution processes. This study presents a numerical analysis on the effects of microwave heating on the mechanical properties of hard rock. In particular, the reduction of the uniaxial compressive and tensile strength of granite-like rock due to microwave irradiation induced damage is numerically assessed.

Rock fracture is modelled by a damage-viscoplasticity model, with separate damage variables for tension and compression types of failure. A global solution strategy is developed where first the electromagnetic problem is solved in COMSOL multiphysics software, then its solution is used as an input for the thermo-mechanical problem, which is finally solved by means of a staggered explicit solution method. Due to the preeminence of the thermal radiation, the thermal and the mechanical parts of the problem are considered as uncoupled.

The model behaviour is tested in 3D finite element simulations of three-mineral numerical rock specimens, with mesostructures explicitly defined, pretreated first in a microwave oven and then subjected to uniaxial compression and tension tests. The results show that the compressive and tensile strength of rock can be considerably reduced by the microwave irradiation pretreatment.

1. Introduction

Rock fracturing is an essential process in the fields of tunnelling, mining, and mineral engineering. Equipment wear during traditional, mechanical fracturing is a commonly found problem that lengthens the duration and raises the costs of the operations. Moreover, rock breakage, especially when encountering hard rocks, is an energy-intensive process. This is particularly significant for rock comminution (crushing and grinding), since it accounts for a large part of the total energy consumption in mining processes (Jeswiet and Szekeres, 2016). Thus, new energy-saving and efficient pretreatment methods, where other physical agents are applied to rocks and ores in order to weaken them before comminution, have been developed in the last decades. One of these methods is thermally assisted liberation by means of microwave irradiation (Kingman and Rowson, 1998).

Microwave energy has been proved to be able to assist mechanical rock fracturing in geotechnical and mining engineering since the 1980s (McGill et al., 1988). The main advantages include high efficiency, immediacy of heating, and no secondary waste (gases and particles) production (Cemhan et al., 2019; Ju et al., 2021). The microwave-induced breakage of rocks benefits from the different microwave absorption capacities of rock constituent minerals, since different dielectric and thermal properties cause thermal gradients and stresses that ultimately lead to tensile failure (Jones et al., 2005). Rock is a heterogeneous material comprising different minerals with differing responses to microwave irradiation. Minerals can be broadly classified in two main categories: the ones transparent to microwaves and the ones which are microwave-absorbent (Chen et al., 1984). Typically, hard heterogeneous rocks such as granite contain mostly poor absorbers, with various degrees of absorption to microwaves. Batchelor et al. (2015) discussed the importance of mineralogy and texture for microwave treatment of metalliferous ores, and they highlighted the role of mechanical properties and, among thermal properties, of thermal expansion coefficient in generating fractures. Besides mineral composition, other factors influencing the heating effect of microwave irradiation on rock are pretreatment duration, microwave power density (Whittles et al., 2003) and frequency (Peinsitt et al., 2010), moisture content, and grain size (Ma et al., 2021).

Numerical studies on thermal microwave-induced fracture of heterogeneous rocks have highlighted the underlying selective heating mechanism. Most of them have focused on 2D systems of two differing mineral phases, one highly absorbent and the other transparent to microwaves. For example, Ali and Bradshaw (2009) used a continuum

* Corresponding author.
E-mail address: martina.pressacco@tuni.fi (M. Pressacco).

https://doi.org/10.1016/j.mineng.2023.108318
Received 8 July 2022; Received in revised form 6 August 2023; Accepted 10 August 2023
Available online 31 August 2023

List of symbols

DP	Drucker–Prager criterion
MR	Modified Rankine criterion
f_{DP}, f_{MR}	DP and MR yield surfaces
g_{DP}	Plastic potential for DP surface
α_{DP}, k_{DP}	DP parameters
$\boldsymbol{\sigma}$	Stress tensor
σ_i	i^{th} principal stress
$\boldsymbol{\varepsilon}^{tot}$, $\boldsymbol{\varepsilon}^{vp}$, $\boldsymbol{\varepsilon}^{\theta}$	total, viscoplastic and thermal strain tensor
I_1	First invariant of stress tensor
J_2	Second invariant of the deviatoric part of stress tensor
c, σ_t	Dynamic cohesion and tensile strength
$\dot{\lambda}_{DP}$, $\dot{\lambda}_{MR}$	Viscoplastic increments for DP and MR surfaces
s_{DP}, s_{MR}	Viscosity moduli for DP and MR surfaces
$\langle\cdot\rangle$	Macaulay brackets
ω_c, ω_t	Damage variables in compression and tension
s_c, s_t	Weighting parameters in compression and tension
ε^{vp}_{eqvc}, ε^{vp}_{eqvt}	Cumulative equivalent plastic strain in compression and tension
G_{Ic}, G_{IIc}	Mode I and II fracture energy
$\mathbf{E}$	Elasticity tensor
EM	Electro-magnetic problem
ϵ_0, ϵ_r	Permittivity of free space and complex relative permittivity
σ_c	Electrical conductivity
ω	Angular frequency
$\mathbf{E}_{EM}$	Electric field
θ	Temperature
k, c_t	Thermal conductivity, specific heat

approach to quantify numerically the damage sustained by microwave-absorbing grains in a non-absorbing matrix due to microwave heating. They found that for a specific ore it may be possible to determine an optimum combination of exposure time and power density which causes the maximum damage. Moreover, the effect of different grain sizes was tested, and it was found that, in order to produce the same damage, more energy is required in the case of finer mineral textures. Ali and Bradshaw (2010) performed computational simulations of microwave heating and thermal damage on two-phase conceptual mineral ores (consisting of 10% galena and 90% calcite) to investigate the most efficient method of microwave power delivery. Their results showed that, under a constant power density, most of the cracks consisted in radially oriented tensile cracks stemming from the boundary of the microwave absorbent phase. It was observed that, for the same power density and mineral percentage, more micro-fractures developed in coarse-grained rock than in fine-grained one. In both cases, higher power densities induced more micro-fractures, especially at the grain boundaries. Jones et al. (2007) studied the effect of microwave power density and exposure time on uniaxial compressive strength (UCS) of a simplified pyrite–calcite system. It was observed that power density had a key role in the reduction of UCS, since thermal stresses increased as power density increased. For equal amounts of input energy, shorter pretreatments yielded larger reductions in strength. However, it was hypothesized the existence of a maximum threshold of power density above which no significant gain in strength reduction is achieved. Wang et al. (2008) tried to estimate the amount of energy saved from applying microwave weakening pretreatment on pyrite–calcite ores with different heating times. It appeared that power density had a large influence on the thermo-mechanical failure of an ore. Furthermore, the results showed that microwave irradiation caused microcracking along the grain boundaries. Wei et al. (2021) determined through the two-dimensional explicit finite difference program FLAC the level of fracture induced during the heating process in a cell model representing an absorbent phase (pyrite) inside a transparent phase (calcite). Microcracking was observed along the grain boundaries of pyrite and calcite. Moreover, radial cracks appeared in the transparent phase and intragranular cracks developed within the absorbent phase.

Compared to the numerous previous 2D studies on fracturing effects of microwave heating of heterogeneous rock systems, fewer fully 3D numerical studies describing explicitly heterogeneity of hard rocks have been conducted in the last ten years. Toifl et al. (2016) conducted a finite difference time domain analysis on two-phase hard rock numerical specimens created in Neper software package to calculate the microwave induced stresses. They extended their previous work to three-phase granite-like cubic numerical specimens and included temperature dependence of material properties (Toifl et al., 2017) . Li et al. (2019) carried out fully-coupled thermo-mechanical simulations in COMSOL Multiphysics to investigate micro-scale stress–strain variability in pegmatite specimens subjected to thermal loading using microwaves. They included heterogeneity by extracting through image processing a thin section from the centre of a standard columnar pegmatite. Xu et al. (2021) applied a statistical distribution to reflect the material heterogeneity in the numerical model and they assumed rock to be elastic and isotropic during microwave heating simulations on cubic hard rock specimens. They formulated a damage-based electromagnetic-thermal and mechanical coupled numerical model was formulated to simulate the damage and fracturing of rock under microwave irradiation.

Despite the advancements in numerical modelling of microwave irradiation effects on rocks and ores brought by the above mentioned studies, they lack, to the best of our knowledge, the modelling of microwave induced damage on heterogeneous hard rock and its weakening effect on rock strength. The present study attempts to provide a preliminary simulation method which comprises both explicit heterogeneity description and damage evaluation. In more detail, the aim of this paper is to evaluate numerically, by 3D simulations, the weakening effect on the uniaxial compressive and tensile strength of polycrystalline hard rock specimens due to microwave irradiation in a multimode oven. A tentative assessment of the method was already carried out in Pressacco et al. (2022), which dealt with 2D simulations of microwave irradiated numerical granite-like specimens. Here those analyses are extended to 3D case to provide more reliable results. This is a three-stage electromagnetic–thermo–mechanical problem, where first a microwave heating pretreatment is applied to granite-like rock specimens, and subsequently conventional mechanical tests are performed on pretreated specimens.

For this scope, the electromagnetic problem is solved first in the commercial FE software COMSOL Multiphysics. Then, a staggered explicit approach is developed to solve the thermo-mechanical problem in MATLAB, where the thermal loading input source is provided by the microwave induced volumetric power density calculated in and exported from COMSOL. The major benefit of this method consists not only in the possibility of defining explicitly the mesostructure (with potential extension to higher levels of complexity, i.e. inclusion of pre-existent defects or pores, etc.), but also the most suitable/convenient modelling of rock breakage. Here rock material heterogeneity is represented explicitly by means of 3D Voronoi tessellations of polyhedral cells, and rock fracturing is modelled by means of a damage-viscoplasticity model. In the numerical simulations, the effect of different random rock mesostructures is taken into account. It should finally be emphasized that this paper is of theoretical-speculative nature, i.e. we do not present any experiments to validate the simulations as we have no access to required laboratory devices. However, we do compare the results, both on microwave irradiation of a granite sample and the weakening effect thereof on the results found in the literature.

2. Rock constitutive model

The theory of the rock constitutive model is described here. The model consists of a viscoplastic and a damage part, as in Saksala (2010). The viscoplastic part defines the stress states leading to rock failure and controls the inelastic deformation. Viscosity allows to render rock strain-rate sensitive. The damage part of the model takes into account the stiffness and strength degradation by means of separate isotropic damage variables in compression and tension, due to the strong asymmetry of rock behaviour. Finally, it should be remarked that the continuum approach based on viscoplasticity and damage mechanics is chosen here for the sake of computational efficiency and simplicity of implementation.

2.1. Bi-surface viscoplastic consistency model

The viscoplastic part of the constitutive model is based on the viscoplastic consistency approach by Wang (1997) and Wang et al. (1997). A bi-surface criterion consisting of Drucker–Prager (DP) criterion for compressive (shear) failure and the modified Rankine (MR) criterion as a tensile cut off define the stress states leading to inelastic strains and damage. The model components for the perfectly viscoplastic case (softening is considered by the damage part) are

$$
\begin{aligned}
&f_{\mathrm{DP}}(\boldsymbol{\sigma},\dot{\lambda}_{\mathrm{DP}}) = \sqrt{J_2} + \alpha_{\mathrm{DP}} I_1 - k_{\mathrm{DP}} c(\dot{\lambda}_{\mathrm{DP}})\\
&f_{\mathrm{MR}}(\boldsymbol{\sigma},\dot{\lambda}_{\mathrm{MR}}) = \sqrt{\sum_{i=1}^{3}\langle\sigma_i\rangle^2} - \sigma_t(\dot{\lambda}_{\mathrm{MR}})\\
&g_{\mathrm{DP}}(\boldsymbol{\sigma}) = \sqrt{J_2} + \beta_{\mathrm{DP}} I_1 - k_{\mathrm{DP}} c_0\\
&\dot{\boldsymbol{\varepsilon}}^{\mathrm{vp}} = \dot{\lambda}_{\mathrm{DP}}\frac{\partial g_{\mathrm{DP}}}{\partial \boldsymbol{\sigma}} + \dot{\lambda}_{\mathrm{MR}}\frac{\partial g_{\mathrm{MR}}}{\partial \boldsymbol{\sigma}}\\
&c = c_0 + s_{\mathrm{DP}}\dot{\lambda}_{\mathrm{DP}}\\
&\sigma_t = \sigma_{t0} + s_{\mathrm{MR}}\dot{\lambda}_{\mathrm{MR}}\\
&f_{\mathrm{DP}} \le 0, \quad \dot{\lambda}_{\mathrm{DP}} \ge 0, \quad \dot{\lambda}_{\mathrm{DP}} f_{\mathrm{DP}} = 0\\
&f_{\mathrm{MR}} \le 0, \quad \dot{\lambda}_{\mathrm{MR}} \ge 0, \quad \dot{\lambda}_{\mathrm{MR}} f_{\mathrm{MR}} = 0
\end{aligned}
\tag{1}
$$

where f_{DP} and f_{MR} are the yield surfaces, g_{DP} is the plastic potential for DP surface (for MR case $g_{\mathrm{MR}} = f_{\mathrm{MR}}$), I_1 is the first invariant of the stress tensor $\boldsymbol{\sigma}$, J_2 is the second invariant of the deviatoric part of stress tensor $\mathbf{s} = \boldsymbol{\sigma} - \frac{\mathrm{tr}(\boldsymbol{\sigma})}{3}\mathbf{I}$, σ_i is the i^{th} principal stress, $\langle\cdot\rangle$ are the Macaulay brackets, i.e. the positive part operator, α_{DP} and k_{DP} are the DP parameters, s_{DP} and s_{MR} are the viscosity moduli (here $s_{\mathrm{DP}} = s_{\mathrm{MR}} = s$, c and σ_t are the dynamic cohesion and tensile strength depending on the viscoplastic increments $\dot{\lambda}_{\mathrm{DP}}$ and $\dot{\lambda}_{\mathrm{MR}}$, respectively. The DP parameters $\alpha_{\mathrm{DP}} = 2\sin\phi/(3-\sin\phi)$ and $k_{\mathrm{DP}} = 6\cos\phi/(3-\sin\phi)$ are defined in terms of the friction angle ϕ. Finally, the parameters β_{DP} and k_{DP} are similar to the ones in Eq. (1) $_1$, but here they depend on the dilatancy angle instead of the friction angle.

2.2. Damage formulation and combining the damage and viscoplastic parts

The largely asymmetric response of rock in tension and compression is taken into account by separate scalar damage variables. The damage in both cases is driven by the viscoplastic strain. As a consequence, the damage part of the model governs both strength and stiffness degradation. In both cases, the standard phenomenological isotropic (scalar) damage model is used with an exponential damage function. Therefore, the damage part of the model is defined by equations

$$
\begin{aligned}
&\omega_c = A_c(1-\exp(-\beta_c\varepsilon^{\mathrm{vp}}_{\mathrm{eqvc}}))\\
&\omega_t = A_t(1-\exp(-\beta_t\varepsilon^{\mathrm{vp}}_{\mathrm{eqvt}}))
\end{aligned}
\quad \text{with}
$$

$$
\beta_c = \frac{\sigma_c h_e}{G_{\mathrm{IIc}}}, \quad \varepsilon^{\mathrm{vp}}_{\mathrm{eqvc}} = \int_0^t \sqrt{\frac{2}{3}\dot{\boldsymbol{\varepsilon}}^{\mathrm{vp}} : \dot{\boldsymbol{\varepsilon}}^{\mathrm{vp}}}\,dt \tag{2}
$$

$$
\beta_t = \frac{\sigma_t h_e}{G_{\mathrm{Ic}}}, \quad \varepsilon^{\mathrm{vp}}_{\mathrm{eqvt}} = \int_0^t \sqrt{\sum_{i=1}^{2}\langle\dot{\varepsilon}^{\mathrm{vp}}_i\rangle^2}\,dt
$$

where ω_c and ω_t are the damage variables in compression (relating to DP criterion) and tension (relating to MR criterion), respectively. Parameters A_c and A_t control their maximum values. Parameters β_c and β_t are defined according to the fracture energies G_{IIc} and G_{Ic}, uniaxial compressive strength σ_c and tensile strength σ_t, and by the characteristic length of a finite element $h_e = \sqrt[3]{6\sqrt{2}V_e}$, V_e being the element volume. The cumulative equivalent viscoplastic strain in compression and tension, $\varepsilon^{\mathrm{vp}}_{\mathrm{eqvc}}$ and $\varepsilon^{\mathrm{vp}}_{\mathrm{eqvt}}$, respectively, are computed incrementally in the algorithmic implementation, and therefore driven by the rate of visco-plastic strain tensor $\dot{\boldsymbol{\varepsilon}}^{\mathrm{vp}}$ (defined in Eq. (2) with the Koiter's rule of bi-surface plasticity and surfaces both active) and its principal values $\dot{\varepsilon}^{\mathrm{vp}}_i$. Furthermore, the colon in Eq. (2) signifies the double contraction operator for tensors, i.e. $\mathbf{A} : \mathbf{A} = A_{ij}A_{ij}$. Macauley brackets are used in the expression of $\dot{\varepsilon}^{\mathrm{vp}}_i$ so that only positive principal strains influence the tensile damage.

The viscoplastic and damage parts of the model are combined in the effective principal stress space. Within this strategy, they are considered independent. Thus, viscoplastic calculations and stress integration are performed first in the effective stress space, independently of damage. Consequently, the robust methods of computational plasticity can be used in the stress integration (Grassl and Jirásek, 2006). Lastly, the nominal–effective stress relationship is defined on the models proposed by Lubliner et al. (1989) and Lee and Fenves (1998)

$$
\begin{aligned}
\boldsymbol{\sigma} &= (1-s_c\omega_t)(1-s_t\omega_c)\bar{\boldsymbol{\sigma}}\\
&= (1-s_c\omega_t)(1-s_t\omega_c)\mathbf{E} : (\boldsymbol{\varepsilon}^{\mathrm{tot}} - \boldsymbol{\varepsilon}^{\mathrm{vp}} - \boldsymbol{\varepsilon}^{\theta})
\end{aligned}
\tag{3}
$$

where $s_c = 1 - w_c(1 - r(\bar{\boldsymbol{\sigma}}))$ and $s_t = 1 - w_t r(\bar{\boldsymbol{\sigma}})$ are functions of the stress state introduced to model elastic stiffness recovery effects associated with stress reversals. This corresponds to the experimentally observed closure of previously present microcracks during initial stages of uniaxial compression (Eberhardt et al., 1999). The parameters $0 \le w_c, w_t \le 1$ are material-dependent weighting factors, with $w_c = 1$, $w_t = 0$ meaning full recovery of elastic stiffness as loading changes from being predominantly tensile to predominantly compressive (for example when applying uniaxial compression tests after thermal pretreatment). Finally, the thermal strain tensor $\boldsymbol{\varepsilon}^{\theta}$ is defined as

$$
\boldsymbol{\varepsilon}^{\theta} = \alpha(\theta)\Delta\theta\mathbf{I} \tag{4}
$$

with α being the thermal expansion coefficient, θ the temperature, and $\mathbf{I}$ the second order identity tensor.

2.3. Stress integration of rock constitutive model

The cutting plane return mapping is used to solve the model in Eqs. (1). When both yield criteria are violated ($f_{\mathrm{MR}} > 0$ and $f_{\mathrm{DP}} > 0$), the consistency conditions (Eq. (1)$_{5,6}$) demand the following equations to be verified at the end of each time step: $f_{\mathrm{MR}}(\boldsymbol{\sigma}^{t+\Delta t}, \dot{\lambda}^{t+\Delta t}) = 0$ and $f_{\mathrm{DP}}(\boldsymbol{\sigma}^{t+\Delta t}, \dot{\lambda}^{t+\Delta t}) = 0$. The yield surfaces are formulated to depend on the increments $\dot{\lambda}_i^{t+\Delta t} = \Delta\lambda_i^{t+\Delta t}/\Delta t$, and the conditions to be satisfied become

$$
f_{\mathrm{MR}}(\boldsymbol{\sigma}^{t+\Delta t}, \Delta\lambda^{t+\Delta t}_{\mathrm{MR}}) = 0, \quad f_{\mathrm{DP}}(\boldsymbol{\sigma}^{t+\Delta t}, \Delta\lambda^{t+\Delta t}_{\mathrm{DP}}) = 0 \tag{5}
$$

The first order expansion of these equations, i.e. the first term of the vector valued Taylor series, produces a linear system for solving the

MR and DP viscoplastic increments:

$$\mathbf{f}(\Delta\boldsymbol{\lambda}+\delta\Delta\boldsymbol{\lambda})=\mathbf{f}(\Delta\boldsymbol{\lambda})+\nabla_{\Delta\boldsymbol{\lambda}}\mathbf{f}(\Delta\boldsymbol{\lambda})\delta\Delta\boldsymbol{\lambda}=\mathbf{0}\Leftrightarrow$$

$$\delta\Delta\boldsymbol{\lambda}=-\nabla_{\Delta\boldsymbol{\lambda}}\mathbf{f}(\Delta\boldsymbol{\lambda})^{-1}\mathbf{f}(\Delta\boldsymbol{\lambda})=\mathbf{G}^{-1}\mathbf{f}(\Delta\boldsymbol{\lambda})$$

$$\Rightarrow \mathbf{G}\delta\Delta\boldsymbol{\lambda}=\mathbf{f} \qquad \text{linear system, with}$$

$$\delta\Delta\boldsymbol{\lambda}=\begin{pmatrix}\delta\lambda_{\mathrm{MR}}\\ \delta\lambda_{\mathrm{DP}}\end{pmatrix},\quad \mathbf{f}=\mathbf{f}(\Delta\boldsymbol{\lambda})=\begin{pmatrix}f_{\mathrm{MR}}(\Delta\lambda_{\mathrm{MR}})\\ f_{\mathrm{DP}}(\Delta\lambda_{\mathrm{DP}})\end{pmatrix}$$

$$\mathbf{G}=\begin{bmatrix}G_{11} & G_{12}\\ G_{21} & G_{22}\end{bmatrix} \tag{6}$$

$$G_{11}=\frac{\partial f_{\mathrm{MR}}}{\partial\boldsymbol{\sigma}}:\mathbf{E}:\frac{\partial f_{\mathrm{MR}}}{\partial\boldsymbol{\sigma}}+\frac{s_{\mathrm{MR}}}{\Delta t}$$

$$G_{12}=\frac{\partial f_{\mathrm{MR}}}{\partial\boldsymbol{\sigma}}:\mathbf{E}:\frac{\partial g_{\mathrm{DP}}}{\partial\boldsymbol{\sigma}}$$

$$G_{21}=\frac{\partial f_{\mathrm{DP}}}{\partial\boldsymbol{\sigma}}:\mathbf{E}:\frac{\partial f_{\mathrm{MR}}}{\partial\boldsymbol{\sigma}}$$

$$G_{22}=\frac{\partial f_{\mathrm{DP}}}{\partial\boldsymbol{\sigma}}:\mathbf{E}:\frac{\partial g_{\mathrm{DP}}}{\partial\boldsymbol{\sigma}}+\frac{s_{\mathrm{DP}}}{\Delta t}k_{\mathrm{DP}}$$

where the components of the gradient $\mathbf{G}$ are obtained by applying the chain rule for the derivatives. After solving the viscoplastic increments by Eq. (6), the stress, viscoplastic strain and internal variables are updated in a standard manner (Wang et al., 1997). For simplicity, the stress integration is performed in the principal stress space. This is viable as the return mapping maintains the principal directions for isotropic materials. Computations at the local integration point level are finally outlined in Box 1. The computations hence start with the total strain $\boldsymbol{\varepsilon}^{\mathrm{tot}}$ from the global solution and end up in the new stress $\boldsymbol{\sigma}$.

Box 1 Solution process for elemental stresses

1: Given $\epsilon^{\mathrm{tot}}_{t+\Delta t}$, $\epsilon^{\theta}_{t+\Delta t}=\alpha\Delta\theta\mathbf{I}$
2: Predict trial elastic stress state
$\bar{\sigma}_{\mathrm{trial}}=\mathbf{E}(\epsilon^{\mathrm{tot}}_{t+\Delta t}-\epsilon^{\mathrm{vp}}_{t}-\epsilon^{\theta}_{t+\Delta t})\longrightarrow$
$\bar{\sigma}^{\mathrm{prin}}_{\mathrm{trial}}=[\bar{\sigma}^{1}_{\mathrm{trial}}\quad\bar{\sigma}^{2}_{\mathrm{trial}}\quad\bar{\sigma}^{3}_{\mathrm{trial}}]$
$f^{\mathrm{trial}}_{\mathrm{MR}}=f_{\mathrm{MR}}(\bar{\sigma}^{\mathrm{prin}}_{\mathrm{trial}},\lambda^{t}_{\mathrm{MR}}),\quad f^{\mathrm{trial}}_{\mathrm{DP}}=f_{\mathrm{DP}}(\bar{\sigma}^{\mathrm{prin}}_{\mathrm{trial}},\lambda^{t}_{\mathrm{DP}})$
3: If ($f^{\mathrm{trial}}_{\mathrm{MR}}$ or $f^{\mathrm{trial}}_{\mathrm{DP}}$) $>0\longrightarrow$
perform viscoplastic correction: calculate $\bar{\sigma}^{t+\Delta t},\varepsilon^{\mathrm{vp}}_{t+\Delta t}$
Else $\longrightarrow$ exit
4: Update damage variables:
$\omega^{t+\Delta t}_{t}=g_{t}(\varepsilon^{\mathrm{vp},t+\Delta t}_{\mathrm{eqvt}}),\quad\omega^{t+\Delta t}_{c}=g_{c}(\varepsilon^{\mathrm{vp},t+\Delta t}_{\mathrm{eqvc}})$
5: Calculate nominal stress:
$\sigma^{t+\Delta t}=(1-\omega^{t+\Delta t}_{t})(1-\omega^{t+\Delta t}_{c})\bar{\sigma}^{t+\Delta t}$

3. Simulation method for microwave heating induced failure

This section outlines the simulation method used here to model microwave heating induced cracking in rock. First, the electromagnetic–thermo–mechanical problem is given in the strong form. The electromagnetic and thermo-mechanical parts are solved separately with a one-way coupling relationship, since, due to lack of reliable and up to date literature data, the dependence on temperature of the dielectric properties is neglected, as similarly as in Toifl et al. (2016) and Wang et al. (2017). The radiative heat is calculated after solving the electric field, and it serves as an input load in the thermo-mechanical problem. The latter becomes an uncoupled problem, due to the highly prevailing role of the radiation-induced internal heat over the heat generated by dissipation effects. Second, the finite element formulation of the strong form is described in brief. Third, a fully explicit (dynamics) solution method based on a staggered approach is presented for solving the finite element discretized version of the thermo-mechanical problem.

3.1. Strong form of the uncoupled electromagnetic–thermo–mechanical problem

Modelling of rock fracturing induced by microwave irradiation requires solving the corresponding electromagnetic–thermo-mechanical problem. The electromagnetic, thermal and mechanical parts of the problem have largely different time scales (Ottosen and Ristinmaa, 2005). By assuming that the electromagnetic cycle periods (in the transient formulation of a time-harmonic EM problem) are short, compared to thermal part time scales, the problem is broken down into two steps. The first step consists in computing the EM radiative losses. For sinusoidal excitations, the EM problem can be solved in the frequency domain to calculate the cycle-averaged losses. In the second step, these losses become a constant input heat source in the time-dependent heat transfer problem.

3.1.1. Formulation of the electromagnetic problem

The electromagnetic part of the problem here is modelled as a wave (i.e. an electromagnetic radiation with frequencies in the microwave range of 300 MHz and 30 GHz Poole and Darwazeh, 2016) propagating in air. The rock sample is placed inside a 2.45 GHz kitchen oven, and it acts as a lossy dielectric object absorbing part of the wave and reflecting and scattering the rest in multiple directions. The Maxwell equation for the electric field strength $\mathbf{E}_{\mathrm{EM}}$ is solved, in COMSOL Multiphysics software, as a time harmonic problem ($\mathbf{E}_{\mathrm{EM}}(x,y,z,t)=\mathbf{E}_{\mathrm{EM}}(x,y,z)e^{j\omega t}$). Mathematically, this equation is (Monk, 2003)

$$\nabla\times\mu_{r}^{-1}\left(\nabla\times\mathbf{E}_{\mathrm{EM}}\right)-k_{0}^{2}\left(\epsilon_{r}-\frac{j\sigma_{\mathrm{EM}}}{\omega\epsilon_{0}}\right)\mathbf{E}_{\mathrm{EM}}=\mathbf{0} \tag{7}$$

where μ_r is the relative permeability, k_0 the wave number of free space, ω is the angular frequency, ϵ_0 is the permittivity of free space, σ_{EM} is the electrical conductivity, $j^2=-1$, and ϵ_r is the relative permittivity. The real part of the complex relative permittivity, $\epsilon_r=\epsilon'_r-j\epsilon''_r$, is the dielectric constant ϵ'_r, and ϵ''_r is the imaginary part, which takes into account the dielectric losses. For air, $\sigma^{\mathrm{air}}_{\mathrm{EM}}=0$, $\epsilon^{\mathrm{air}}_{r}=1-j\cdot 0$, $\mu^{\mathrm{air}}_{r}=1$. Here, material properties are considered to be independent of temperature due to the lack of solid and up to date dielectric properties versus temperature curves. Moreover, a temperature rise below the $\alpha-\beta$ transition of Quartz point (573 °C) does not seem to impact significantly the dielectric properties of granite (Hartlieb et al., 2016), which is the rock type considered here.

Perfect electric conductor (PEC) boundary condition $\mathbf{n}\times\mathbf{E}_{\mathrm{EM}}=\mathbf{0}$ is applied on the cavity walls, where $\mathbf{n}$ is the normal vector on the walls. Dimensions of the waveguide joined to the RF source (magnetron) frequency are such that the waveguide runs with its dominant TE_{10} mode (Pozar, 2011). An electromagnetic wave loses some of its energy when advancing through a lossy dielectric medium. This electromagnetic energy is converted into thermal energy within the medium. Thus, P_v is the time-averaged volumetric power density absorbed by a dielectric medium in an electro-magnetic field, determined in this case as (Haus and Melcher, 1989; Jackson, 1998)

$$P_{v}=\frac{\omega}{2}\epsilon_{0}\epsilon''_{r}E^{2}_{\mathrm{EM}}(x,y,z) \tag{8}$$

Then, the power density term accomplishes the one-way coupling of the EM field with the temperature field in the balance of energy equation, as can be seen in Section 3.1.2.

3.1.2. Formulation of the thermo-mechanical problem

After the solution of the electromagnetic part of the problem, the strong form of the global balance equations for the thermo-mechanical problem can be expressed as

$$\begin{cases}\rho\ddot{\mathbf{u}}=\nabla\cdot\boldsymbol{\sigma}+\mathbf{b} & \text{force equilibrium}\\ \rho c_{t}\dot{\theta}=-\nabla\cdot\mathbf{q}+Q_{\mathrm{int}}+P_{v} & \text{balance of energy}\end{cases} \tag{9}$$

where ρ is the material density, $\mathbf{b}$ is the body force (per unit mass) vector, P_v is the previously defined power density, and c_t is the specific

heat. The constitutive equation for the conductive heat flow, which associates the heat flux to the temperature, is Fourier's law $\mathbf{q} = -k\nabla\theta$, where k is the thermal conductivity and θ the temperature. Finally, Q_{int} is the thermo-mechanical coupling term that accounts for the mechanical heating and thus includes thermo-elasticity and thermo-plasticity effects in the material.

The coupled thermo-mechanical problem can be significantly reduced due to the nature of the microwave heating induced breakage of rock. More specifically, the order of magnitude of the temperature rise caused by microwave irradiation in this study is hundreds of degrees centigrade. Therefore, the thermo-elastic effects in the bulk continuum material can be overlooked as their order of magnitude is about 0.1 °C (Ottosen and Ristinmaa, 2005). Moreover, the temperature rise in a fully developed shear band during a typical experimental compression test on rock is only few degrees centigrade (Saksala et al., 2019). Therefore $Q_{\text{int}} \equiv 0$ follows, and the solution of the problem defined by Eq. (9) becomes remarkably simpler, as the temperature rise at material point level can be ignored.

3.2. Finite element discretized form for the uncoupled thermo-mechanical problem

The finite element formulation for the heat balance equation becomes, following Ottosen and Ristinmaa (Ottosen and Ristinmaa, 2005),

$$\mathbf{C}\dot{\boldsymbol{\theta}} + \mathbf{K}_\theta\boldsymbol{\theta} - \mathbf{f}_\theta = \mathbf{0} \tag{10}$$

where $\boldsymbol{\theta}$ is the nodal temperature vector, $\mathbf{C}$, $\mathbf{K}_\theta$ and $\mathbf{f}_\theta$ are the capacity matrix, the conductivity matrix and the external force vector, respectively, defined by the following expressions:

$$\begin{aligned}
\mathbf{C} &= \mathop{\mathsf{A}}_{e=1}^{n_{el}} \int_{V^e} \rho c_t \mathbf{N}_\theta^{e\mathrm{T}} \mathbf{N}_\theta^e dV \\
\mathbf{K}_\theta &= \mathop{\mathsf{A}}_{e=1}^{n_{el}} \int_{V^e} k \mathbf{B}_\theta^{e\mathrm{T}} \mathbf{B}_\theta^e dV \\
\mathbf{f}_\theta &= \mathop{\mathsf{A}}_{e=1}^{n_{el}} \int_{V^e} \mathbf{N}_\theta^{e\mathrm{T}} P_v dV
\end{aligned} \tag{11}$$

where c_t and k are the specific heat and conductivity, $\mathbf{N}_\theta$ is the temperature interpolation vector, P_v is the volumetric power density in the solid induced by microwave heating, and $\mathbf{B}_\theta^e$ is the gradient of the temperature interpolation vector. Finally, A is the standard finite element assembly operator.

The mechanical problem is governed by the finite element discretized equation of motion

$$\begin{aligned}
&\mathbf{M}\ddot{\mathbf{u}} + \mathbf{f}^{\text{int}}(\theta, \mathbf{u}) = \mathbf{f}^{\text{ext}} \qquad \text{with} \\
&\mathbf{f}^{\text{int}}(\theta, \mathbf{u}) = \mathop{\mathsf{A}}_{e=1}^{n_{el}} \int_{V^e} \mathbf{B}_u^{e\mathrm{T}} \boldsymbol{\sigma}(\theta, \mathbf{u}) dV
\end{aligned} \tag{12}$$

where $\mathbf{M}$ is the lumped mass matrix, $\mathbf{f}^{\text{ext}}$ is the external force vector, $\mathbf{B}_u^e$ is the kinematic matrix, and $\boldsymbol{\sigma}$ is the stress vector defined in Eq. (3).

3.3. Solution methods for the global thermo-mechanical problem

An isothermal split is then applied to the uncoupled thermo-mechanical problem so that the thermal and mechanical parts are solved independently. An explicit–explicit scheme is thus developed by using the staggered approach in order to solve the global thermo-mechanical part of the problem (see Fig. 1). Here, the mechanical part is solved as a quasi-static problem, which is justified by the negligible inertia effects during microwave heating. Staggered schemes are treated more comprehensively in Ottosen and Ristinmaa (2005), Ngo et al. (2014), Felippa and Park (1980) and Martins et al. (2017). For modelling uniaxial compression and tension tests that are to be performed after solving the microwave heating problem, an explicit time marching scheme is adopted.

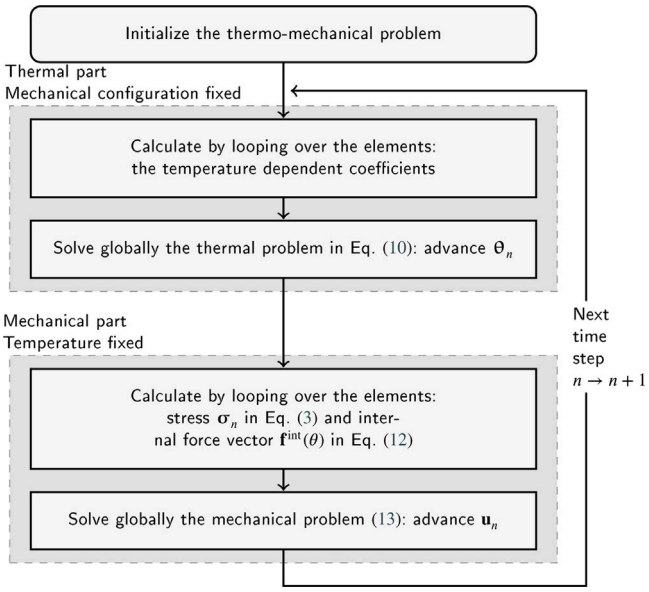

Fig. 1. Explicit–explicit dynamic time integration scheme for the thermo-mechanical problem.

3.3.1. Explicit scheme for the uniaxial compression and tension tests

The explicit modified Euler time integration scheme is chosen for this problem. The equation of motion (Eq. (12)) for the acceleration is solved as

$$\ddot{\mathbf{u}}_n = \mathbf{M}^{-1}(\mathbf{f}_n^{\text{ext}} - \mathbf{f}_n^{\text{int}}(\theta, \mathbf{u}_n)) \tag{13}$$

then the response is advanced by (Hahn, 1991)

$$\dot{\mathbf{u}}_{n+1} = \dot{\mathbf{u}}_n + \Delta t \ddot{\mathbf{u}}_n \tag{14}$$

$$\mathbf{u}_{n+1} = \mathbf{u}_n + \Delta t \dot{\mathbf{u}}_{n+1} \tag{15}$$

As all explicit time integrators, this scheme is conditionally stable with respect to time step Δt. The time step is restricted by the Courant limit and can be easily calculated.

4. Numerical simulation: results and discussion

This section displays the 3D numerical simulations of microwave heating and subsequent mechanical tests. The effect of mesostructure variation will be tested. Moreover, due to the qualitative and preliminary quantitative aspect of this analysis, proper validation of the numerical simulations will be postponed in future studies of the method.

4.1. Numerical simulation: results and discussion

Material heterogeneity is an essential feature that needs to be considered when studying cracking behaviour of rocks, since it has a large influence on the mechanical response of rock during both thermal and mechanical loading. The inherent heterogeneity of granite-like rock here is explicitly described at grain scale by a mesostructure representing constituent minerals aggregation and distribution. This is rendered through a Voronoi tessellation of convex polyhedra (or cells, here the equivalent of mineral grains). In this study, the software package for polycrystal generation Neper by Quey et al. (2011) is used for the creation of the grain texture. The numerical rock samples generated with this method are three 10 000-cell cylinders with a diameter of 40 mm and height of 80 mm, henceforth referred to as Mesostructure 1, 2, and 3 (see Fig. 2a). They are constituted of three minerals (i.e. 30%

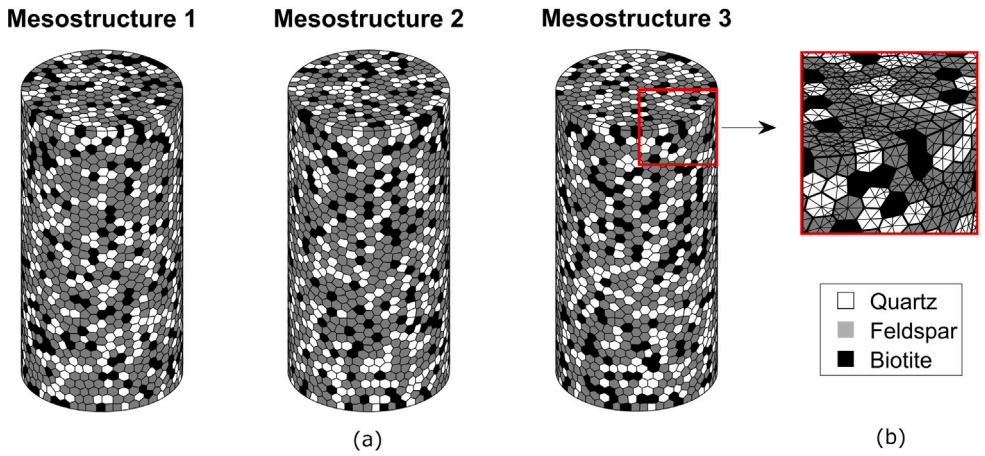

Fig. 2. Numerical rock samples (a) and enlarged detail (b) of the grains (10 000 polyhedra) and linear tetrahedra mesh (972 289 elements).

Table 1
Material properties and model parameters used in simulations.

Parameter			Quartz	Feldspar	Biotite
	Percentage in the sample	[%]	30	55	15
ρ	(Density)	[kg/m^3]	2650	2620	3050
E	(Elastic modulus)	[GPa]	80	60	20
ν	(Poisson's ratio)		0.17	0.29	0.20
σ_t	(Tensile strength)	[MPa]	10	8	7
c	(Cohesion)	[MPa]	25	25	25
ϕ	(Internal friction angle)	[°]	50	50	50
G_{Ic}	(Mode I fracture energy)	[J/m^2]	40	40	28
G_{IIc}	(Mode II fracture energy)	[J/m^2]	$10G_{Ic}$	$10G_{Ic}$	$10G_{Ic}$
α	(Thermal expansion coefficient)	[1/K]	1.60×10^{-5}	0.75×10^{-5}	1.21×10^{-5}
k	(Thermal conductivity)	[W/mK]	4.94	2.34	3.14
c_t	(Specific heat capacity)	[J/kgK]	731	730	770
ε'	(Dielectric constant)		4.72	5.55	7.48
ε''	(Loss factor)		0.014	0.118	0.456

quartz, 55% feldspar and 15% biotite) to reproduce a generic granite-like rock (Vázquez et al., 2015). After meshing the geometry with linear tetrahedral finite elements (see Fig. 2b), a certain number of cells is randomly selected according to these percentages and the clusters of elements inside them are assigned with mineral-specific material properties.

The values of the mineral properties (for intact rock at room temperature) are given in Table 1. Dielectric properties are from Zheng et al. (2020), and for simplicity they are considered constant during the solution of the electromagnetic problem. Mechanical properties for the different minerals are taken mainly from Mahabadi (2012), whereas the values for density, thermal conductivity and specific heat are taken from Schön (2011), Clauser and Huenges (2013), and Waples and Waples (2004), respectively. Lastly, the viscosity is set to 0.005 MPa s m^{-1}, a value large enough to stabilize the computations and small enough not to generate significant strain rate effects at low-velocity loading.

Temperature dependence of certain material parameters is taken into account, since temperature rise due to microwave irradiation is hundreds of degrees. It is remarked that the temperature levels are not sufficient to cause phase changes, such as $\alpha - \beta$ transition of Quartz at 573 °C. In the present study, Young's modulus, tensile and shear strengths are assumed to depend linearly on temperature in the temperature range from 20 to 500 °C - an assumption justified for granites (Homand-Etienne and Houpert, 1989; Vosteen, 2003). Mathematically, this linear dependence is defined as

$$x(\theta) = x(\theta_{\text{ref}}) + K_x^{500}(\theta - \theta_{\text{ref}}) \quad \text{with}$$
$$K_x^{500} = \frac{x(500\,^\circ\text{C}) - x(\theta_{\text{ref}})}{500\,^\circ\text{C} - \theta_{\text{ref}}} \tag{16}$$

where K_x^{500} is the modulus of temperature dependence and $\theta_{\text{ref}} = 20\,^\circ$C is the reference temperature. Moreover, the values at $\theta = 500\,^\circ$C are extrapolated from the fitting lines of the temperature dependence curves for these material properties (Wang and Konietzky, 2019)

$$\begin{aligned} E(500\,^\circ\text{C}) &= 0.45E(\theta_{\text{ref}}) \quad \text{Young's modulus} \\ \sigma_t(500\,^\circ\text{C}) &= 0.50\sigma_t(\theta_{\text{ref}}) \quad \text{tensile strength} \\ c(500\,^\circ\text{C}) &= 0.70c(\theta_{\text{ref}}) \quad \text{cohesion} \end{aligned} \tag{17}$$

However, temperature dependence of thermal expansion coefficient of granite is nonlinear, and it can be approximated by the power function (see Wang and Konietzky, 2019)

$$\alpha(\theta) = (0.8383 - 0.00142\theta)^{-1/1.7085}\alpha(\theta_{\text{ref}}) \tag{18}$$

where $\alpha(\theta_{\text{ref}})$ is the value of the coefficient of thermal expansion of minerals at initial temperature (20 °C) and θ is the temperature expressed in Celsius degrees.

4.2. Uniaxial compression tests on intact numerical rock samples

Uniaxial compression tests are performed on intact numerical rock samples first in order to find their initial compressive strengths and failure modes. During mechanical tests, the sample is simply supported at the bottom, and a constant velocity of 0.05 m/s is applied at the top side, resulting in a strain rate of 1 s^{-1}. This loading rate is chosen since it is within the range of strain rates in drop weight test machines representing thus the low-velocity impact comminution. Moreover, at this level the dynamic increase factor (DIF) is still very modest (less than 1.5) (Zhang and Zhao, 2014), The explicit time integration in Eqs. (13)–(15) is used here. The weighting factors in Eq. (3) w_c, w_t are both set to zero. The results of these simulations are shown in Figs. 3 and 4.

Fig. 3 shows the resulting damage in terms of tensile and compressive damage variables (ω_t and ω_c in Eq. (2)) for Mesostructure 1 at failure. The predicted final failure mode is shearing along few planes, a failure mode experimentally observed in Basu et al. (2013). The stress–strain response in terms of volumetric strain is first compactant and then dilatant (Jaeger et al., 2007), in accordance with the typical experimental behaviour (Mardalizad et al., 2018). According to these simulation results, the present damage-viscoplasticity predicts the essential features of rock under uniaxial compression, i.e. a feasible failure mode and stress–strain response.

Shear failure modes, with differing details, can be observed also for the other two intact numerical samples (Mesostructure 2 and 3 in Fig. 2). The average axial stress–strain curves shows very little variation in the compressive strengths values, with a value of 108 MPa for all

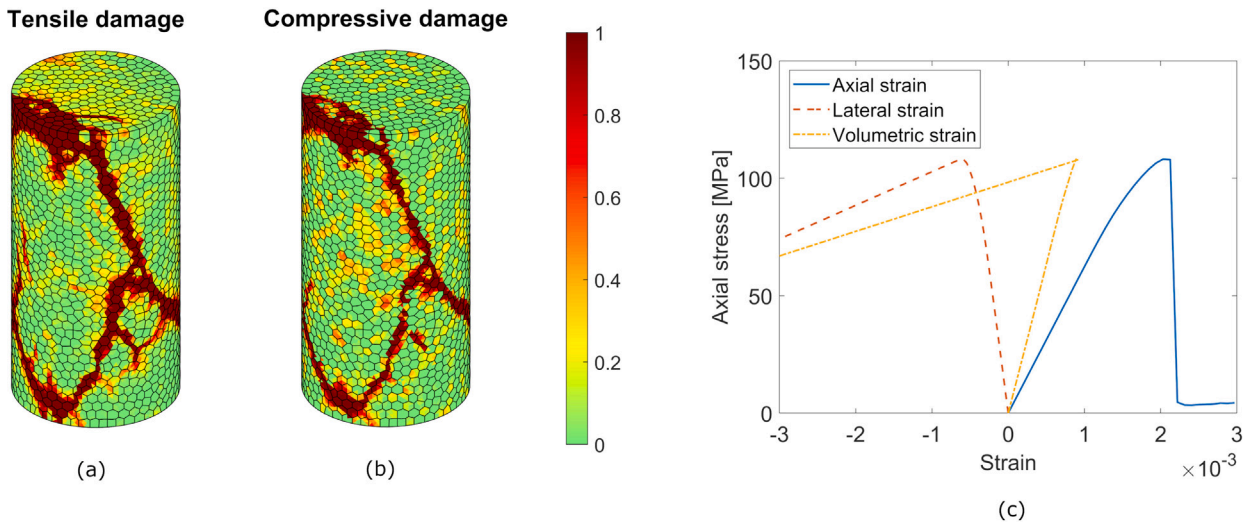

Fig. 3. Uniaxial compression test simulation results for intact rock samples (Mesostructure 1). Failure modes represented as damage patterns and variables (a)–(b). Axial stress–strain curve (c).

three mesostructures. This is likely due to the regular nature of the centroidal Voronoi tessellation created in Neper, which leads to almost identical geometries. Thus, in order to reproduce the experimental deviation in compressive strength of rock (Tang and Hudson, 2010), more irregular tessellations should be chosen. It is also remarked that under dynamic loading the response of brittle materials becomes more deterministic with higher load rates, i.e. increasing loading rates give smaller deviations from the mean value (Denoual and Hild, 2000).

4.3. Microwave pretreatment on numerical rock samples

In this section the effect (in terms of temperature rise and resulting damage) of microwave heating pretreatment is tested on intact numerical samples, with the boundary conditions defined in Section 4.1. The effect of different mesostructures (Fig. 2) is tested. The oven power is set to 1.2 kW, and the frequency is 2.45 GHz. The pretreatment duration is 60 s.

4.3.1. Microwave pretreatment on numerical rock samples: reference case

For microwave irradiation pretreatment, the numerical rock sample is placed in an oven represented by a conductive box connected to a microwave source located at a side of the cavity. The RF power is fed via a waveguide (WR340). The 2.45 GHz frequency is the standard operating frequency of kitchen ovens, and also the power level is in the typical range of commercial ovens (0.8 kW–1.8 kW). Cavity size is $276 \times 254 \times 185$ mm. The outer, boundary surface of the specimen is considered insulated with respect to the surrounding air, therefore all convective effects are neglected. The sample is not restrained from deforming during heating and its initial temperature is 20 °C. The cylinder is placed at the centre of the cavity along the y and z directions. In x direction, a trial-and-error method is used to find the best positioning for this particular oven-sample combination. Fig. 5 shows the oven setup and specimen positioning inside the oven. The distance between the waveguide opening and the leftmost point of the sample in x direction is 12 cm. This distance is the one that yields, at the end of the pretreatment, the highest average value of the nodal temperatures inside the whole sample. Fig. 6 shows the development of the average value of the nodal temperatures inside the sample vs. time for different distances of the leftmost point of the sample from the waveguide opening. The tested distances range from 0 cm to 21 cm with increments of 3 cm (i.e. 0 cm, 3 cm, 6 cm, etc.).

The first simulation is conducted with Mesostructure 1 (Fig. 2) using the explicit solution scheme of Section 3.3.1. Mass scaling is applied to increase the critical time step (from 6×10^{-9} s to 6×10^{-5} s), with a large scaling factor justified by the quasi-static nature of the very slow heating of the rock sample (Pressacco and Saksala, 2020). The weighting factors in Eq. (3) w_c, w_t are both set to zero. To solve the electromagnetic problem, the rock mesostructure, after being created in software package Neper, is exported to commercial FE solver COMSOL Multiphysics software in STL format. There, the polygonal Voronoi cells are meshed with the linear tetrahedral finite elements. Finally, after solving the electromagnetic problem in COMSOL, the nodal vector of generated heat values is exported from COMSOL to MATLAB, where the external force vector in Eq. (11) is assembled and the solution of the thermo-mechanical problem is achieved. The flowchart of the solution method is given in Fig. 7. Figs. 8–10 show the simulation results.

At the end of the pretreatment, the electric field norm is in accordance in terms of qualitative distribution (presence of hotspots typical of multimode ovens, see Fig. 8) and order of magnitude with previous studies that used similar microwave setups and material dielectric properties (Hassani et al., 2011; Santos et al., 2010; Shadi et al., 2022). As is typical in multimode microwave ovens (Mehdizadeh, 2015), the electric field norm distribution is not uniform (Fig. 9a-b). As a consequence, two high-temperature hotspots occur in the sample (Fig. 9d), one at the side that faces directly the waveguide, and the other at the opposite side. The maximum temperature reached in the sample is 392 °C.

The predicted tensile damage patterns in Fig. 10c consist of three horizontal crack-like damage areas on the specimen outer surface. The resulting compressive damage is negligible, therefore it is not shown here. At this temperature level, the value of tensile damage parameter is close to 1 therein so that these zones can be interpreted as macrocracks. These results are analogous (given the same temperature levels) to the ones obtained in the preliminary 2D analysis in Pressacco et al. (2022) in terms of damage shape, orientation, and position.

Circumferential crack patterns have been observed experimentally in several previous studies. Hartlieb (2013) noticed this type of cracks in a drill core taken from a Neuhaus granite spot irradiated for 72 s with a 25 kW continuous wave. In Nicco et al. (2020) Pikes Peak biotite granite cylindrical samples were heated from 60 to 300 s at 2.45 GHz and 3.2 kW in a multimode oven. Hao et al. (2020) irradiated magnetite blocks in a high-temperature microwave muff furnace for 5 min at 2 kW and evaluated the effect of natural cooling at room temperature versus water spray cooling. In Kahraman et al. (2020) circumferential cracks were produced in cylindrical granite and syenite specimens after 360 s at 6 kW in an industrial microwave oven. Shale samples were heated

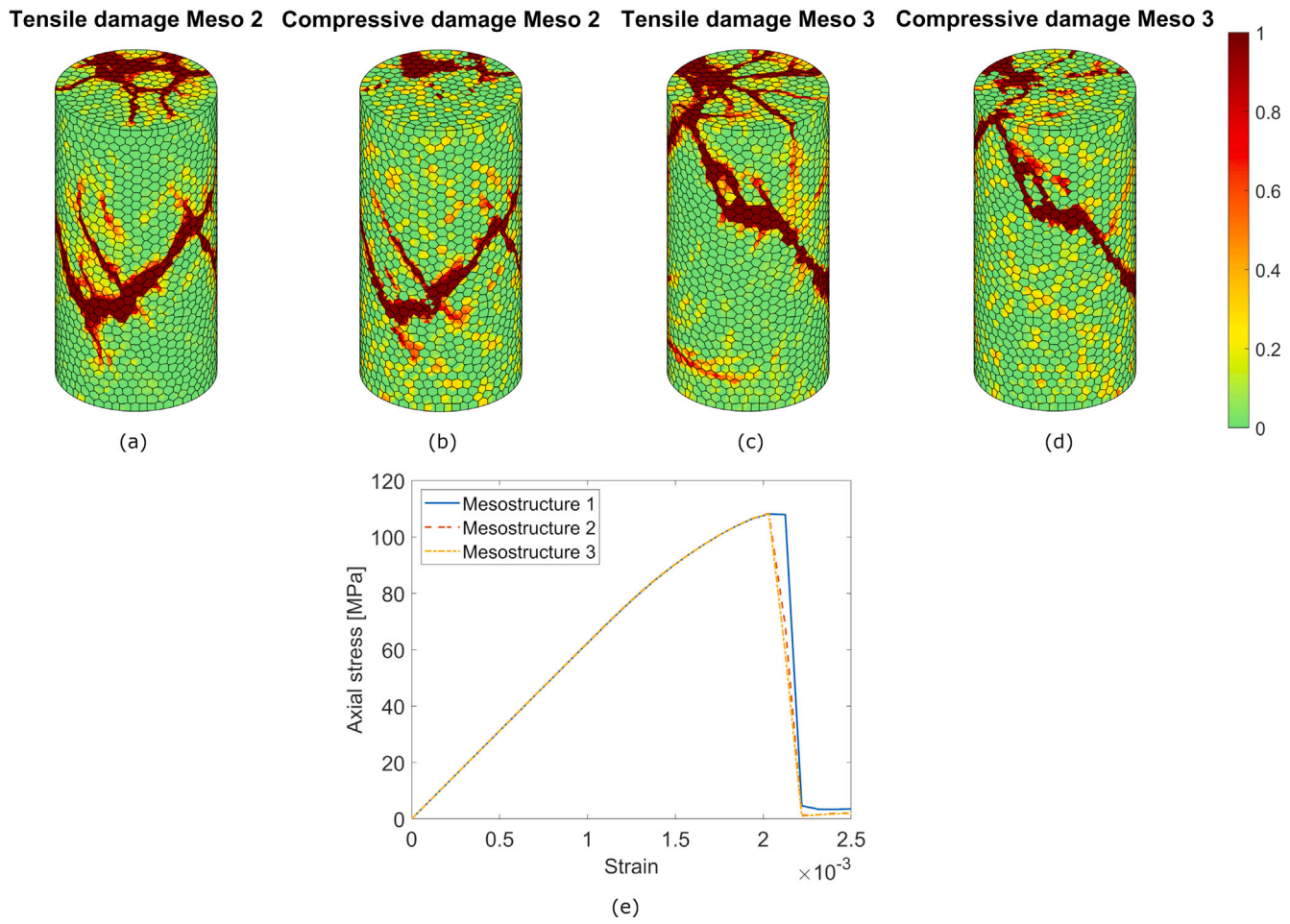

Fig. 4. Uniaxial compression test simulation results for intact rock samples (Mesostructure 2 and 3). Failure modes represented as damage patterns and variables (a)–(d). Corresponding axial stress–strain curves for Mesostructure 1, 2 and 3 (e).

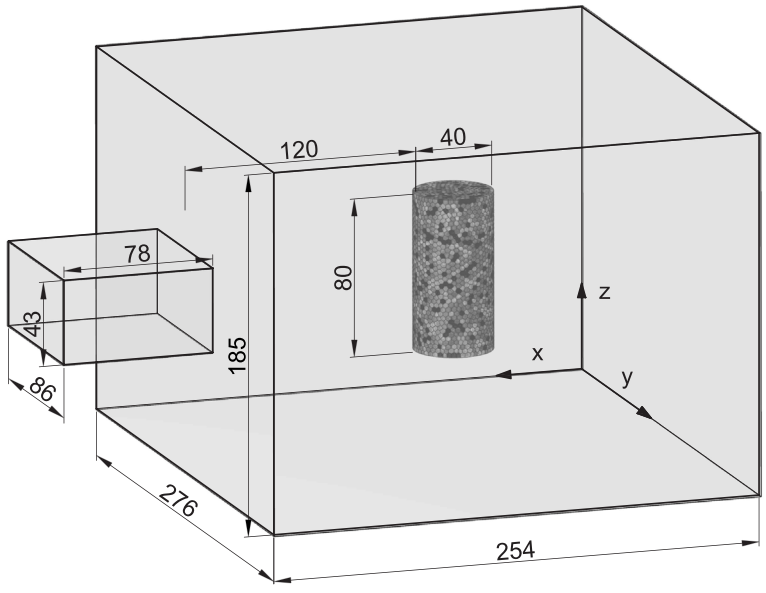

Fig. 5. Oven and waveguide schematic (with d = 120 mm).

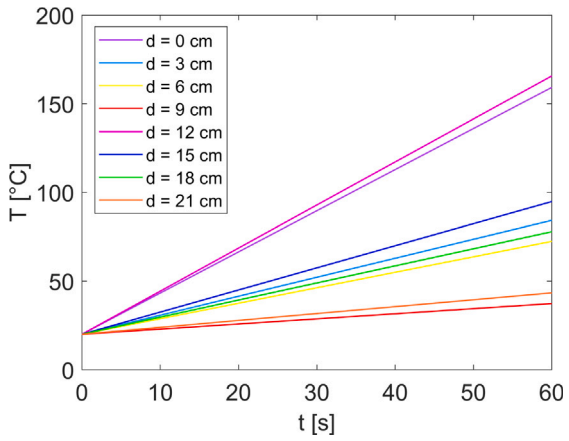

Fig. 6. Average nodal temperatures inside the sample vs. time for different distances from the waveguide opening.

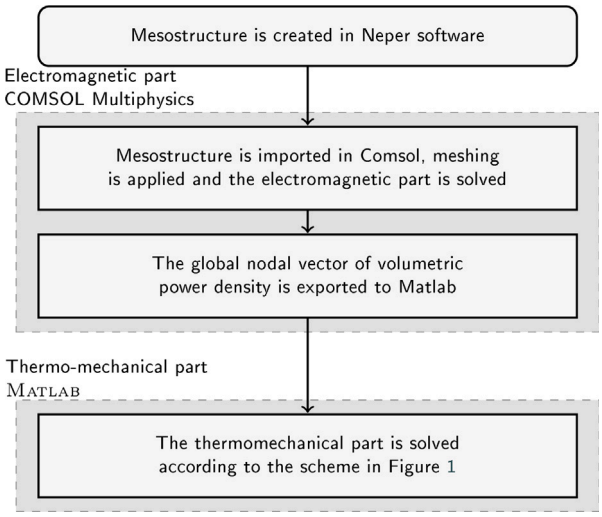

Fig. 7. Explicit–explicit dynamic time integration scheme for the thermo-mechanical problem.

in Chen et al. (2021) by a household microwave oven at 0.7 kW during many time steps of increasing length. In Gao et al. (2022) cylindrical granite samples were irradiated for several minutes up to high temperatures until melting of the transversal cross section of the cylinders. Therefore, as the damage patterns due to microwave pretreatment were qualitatively akin to those predicted here, these experimental results lend some validation on the present simulations.

Finally, it can be noted that damage affects primarily feldspar, and secondly biotite, with almost no damage in quartz. An analogous result was found also in Inserra et al. (2013), where thermal damage due to heating/cooling cycle at different high temperatures was observed by ultrasonic measurements. Their results showed that the number of cracks was higher in feldspar, compared to quartz. In the present study, this could be explained by the higher values of the thermal expansion coefficient for quartz and biotite compared to the one of feldspar. The differential expansion and contraction of minerals induces higher stresses in the ones with a lower thermal expansion coefficient (Molaro et al., 2015). Moreover, the higher values of dielectric properties of biotite lead to a faster heating in this mineral, which cause thermal stresses and consequently tensile cracks in the surrounding grains (Ge et al., 2021).

4.3.2. Microwave pretreatment on numerical rock samples: influence of mesostructure

To test the effect of heterogeneity, the reference simulation case in Section 4.3.1 is carried out with Mesostructure 2 and 3 (Fig. 2). The simulation results for temperature distribution and induced damage patterns are shown in Fig. 11.

In all three cases the results are quite similar. Temperature distribution plots, not shown here, display qualitatively the same two-hotspots distribution. The maximum temperature reached in the sample is comparable to the one of Mesostructure 1, being 370 °C and 366 °C for Mesostructure 2 and 3 respectively. The damage patterns show the same behaviour for all three specimens, with three main horizontal, transversal tensile damage areas. The compressive damage is again negligible and is not shown here.

4.4. Uniaxial compression and tension tests on microwave irradiated numerical samples

This section presents the simulations of mechanical tests conducted on microwave pretreated numerical samples. The uniaxial compression test simulations are carried out on irradiated numerical samples cooled down back to room temperature. Therefore, it is assumed that the thermal stresses and deformations are zero at the initial state of the mechanical tests. However, the damage induced by the microwave heating pretreatment is present. This represents the in-situ comminution case where a considerable time has passed between the microwave heat treatment and the mechanical breakage.

4.4.1. Uniaxial compression on microwave irradiated numerical samples: reference case

Uniaxial compression tests are conducted on the microwave pretreated numerical sample of Section 4.3.1. The simulation results for failure modes and stress–strain response are shown in Fig. 12. The mechanical test is performed on the pretreated sample first with the weighting factor in Eq. (3) $w_c = w_t = 0$ as in microwave irradiation, then with $w_c = 1$ and $w_t = 0$ to simulate microcrack closure and full elastic stiffness recovery during initial stages of uniaxial compression. The results are then compared.

The damage patterns in Fig. 12(a)-(d) show that for $w_c = 0$ the failure mode is realized through an extension of the main damage area in the pretreated sample through the entire cylinder. When $w_c = 1$ the effect of tensile damage variable ω_t (see Eq. (3)) is continuously limited by the parameter $0 < s_c \leq 1$ during uniaxial compression. As a consequence, a more ductile behaviour occurs and the achieved compressive strength is higher than the one for $w_c = 0$ (see Fig. 12e). Moreover, a more beneficial effect in terms of uniaxial compressive strength reduction is obtained for $w_c = 0$ (55 MPa) compared to $w_c = 1$ (89 MPa), resulting in a 49 % and a 18 % reduction of the initial compressive strength. These reduction percentages are in accordance with the ones obtained in the earlier 2D analysis in Pressacco et al. (2022), where the maximum reduction in strength, when neglecting stiffness recovery, was 38 % of the initial one.

These strength reduction percentages agree, to some extent, with those obtained by Kahraman et al. (2020). There, after thermal pretreatment for 360 s at 6 kW in an industrial microwave oven, similar surface temperatures between 300 °C and 400 °C were reached in several granites (Steppe yellow, Rosa minho, and Nublado types). The initial uniaxial compressive strengths of these granites were in the 130 MPa–150 MPa range. The reduction in strength due to thermal pretreatment varied between 15 % and 43 %, therefore providing results compatible to the ones obtained in this study. Moreover, similar crack patterns were found in Hao et al. (2020). There, the failure modes caused by drop hammer comminution test after microwave irradiation were somewhat comparable to the ones predicted here. However, the much higher loading rate therein resulted in multiple macrocrack planes. The strength reduction of irradiated samples let to cool down naturally at room temperature varied from 20 % to 30 %.

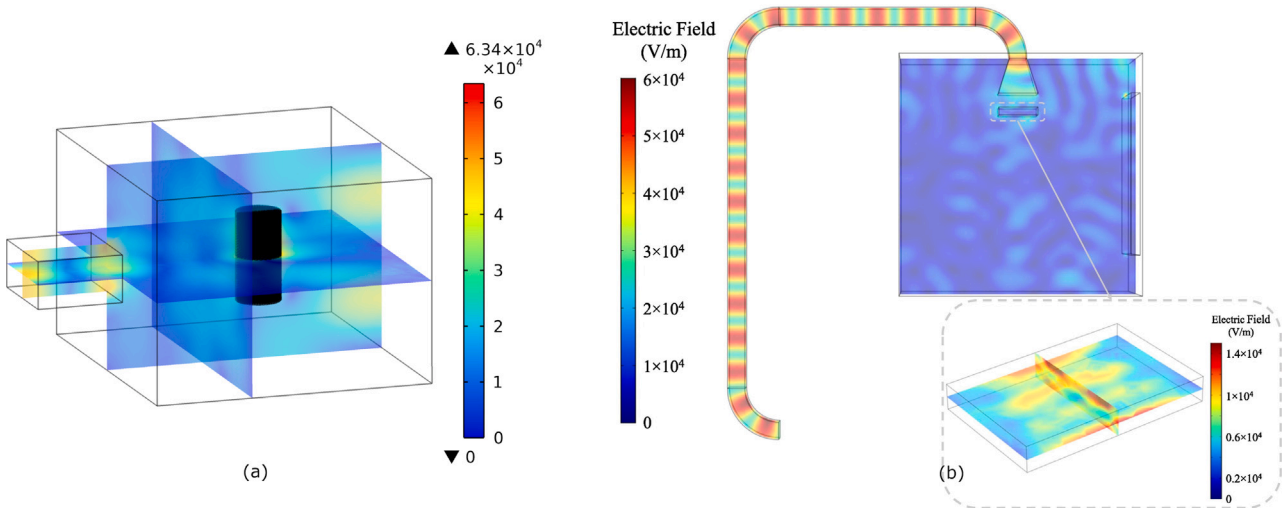

Fig. 8. Microwave pretreatment simulation results (reference case: Mesostructure 1). Electric field norm in the oven and in the sample (a). Electric field norm in a microwave oven and in a basalt slab treated with 3 kW microwave power for 4.35 s (Shadi et al., 2022).

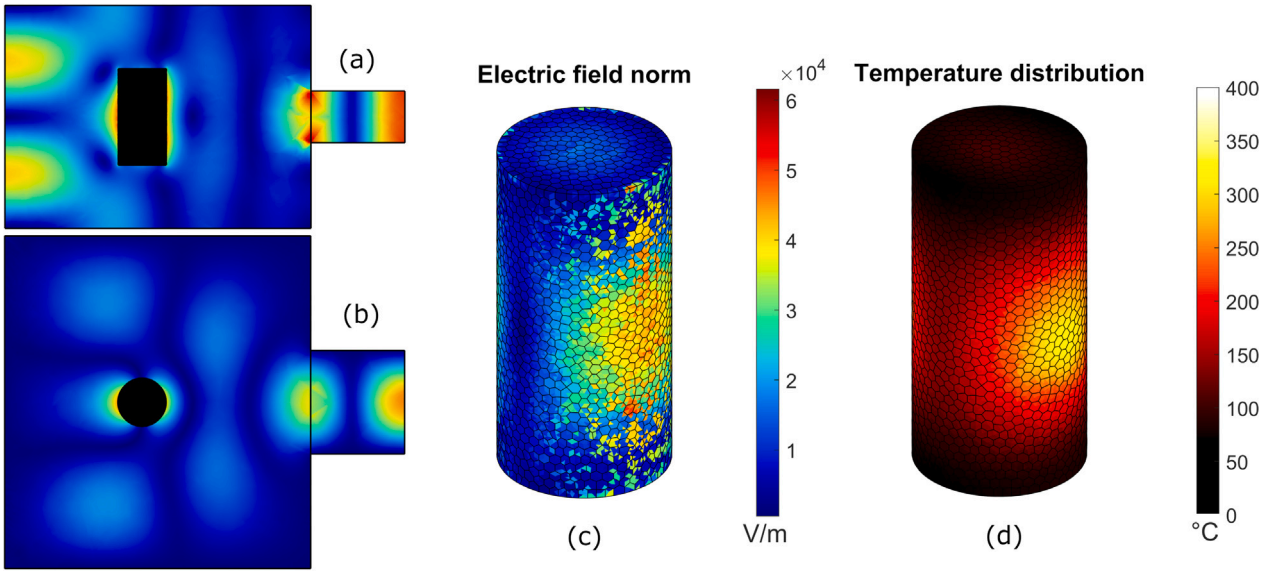

Fig. 9. Microwave pretreatment simulation results (reference case: Mesostructure 1). Electric field norm in the oven along xz plane (a), xy plane (b), electric field norm in the sample (c), and temperature distribution in the sample (d) at 60 s.

4.5. Tension test on microwave irradiated numerical samples

Finally, in this section, a numerical tension test is carried out on an intact sample with Mesostructure 1 and on a pretreated sample with the same mesostructure. The simulation results for intact and pretreated cases with a velocity applied at the top of 0.05 m/s are shown in Fig. 13.

The simulation results for the uniaxial tension test at velocity 0.05 m/s shown in Fig. 13 prove that the model can predict the experimental transversal splitting mode with a single macrocrack. The resulting tensile strength is about 8 MPa, which is close to the homogenized tensile strength of 8.45 MPa (calculated by simple rule of mixtures). The failure mode of the pretreated sample occurs by transversal extension of the largest microwave induced circumferential crack. The corresponding tensile strength is about 1.75 MPa, which is 21 % of the intact value. Finally, the stress–strain response in Fig. 13c shows a lower value of tangent modulus and a more ductile post-peak response. It can then be concluded that the present type of microwave heating pretreatment can be an effective way to weaken rock under tensile loading.

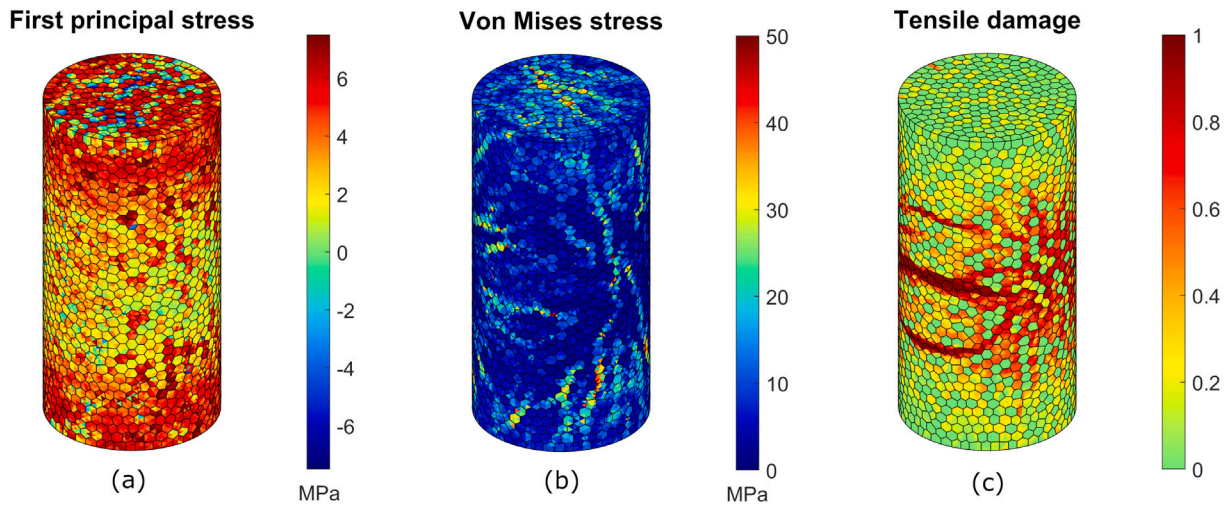

Fig. 10. Microwave pretreatment simulation results (reference case: Mesostructure 1). First principal stress and Von Mises stress at 60 s (a)–(b). Failure modes represented as distributions of tensile damage variable at 60 s (c).

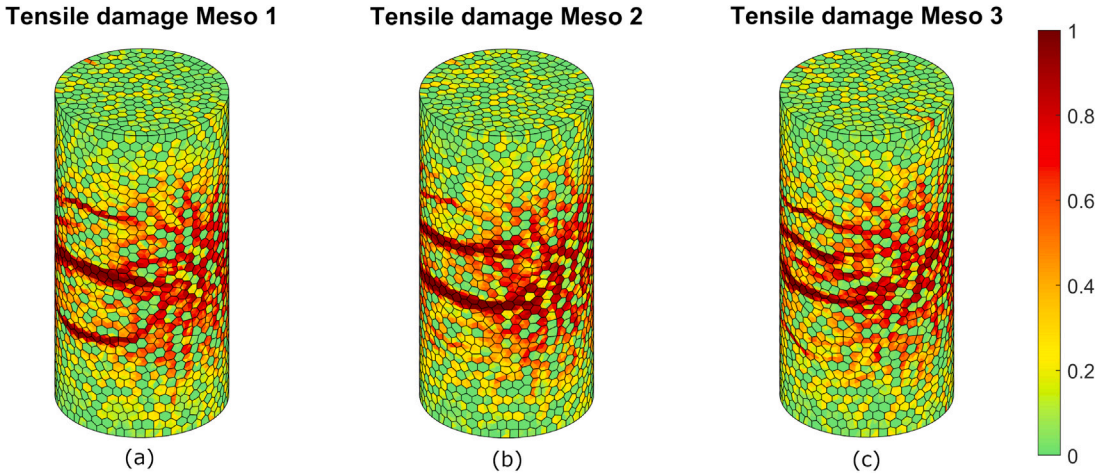

Fig. 11. Simulation results for microwave pretreated samples (Mesostructure 1, 2 and 3).

5. Conclusions

A continuum approach-based method to simulate microwave heating assisted rock fracture was developed and tested in this paper. Rock failure was modelled by a damage-(visco)plasticity model based on Rankine and Drucker–Prager yield criteria, while strength and stiffness degradation was taken into account by means of separate scalar damage variables in tension and compression. Moreover, the unilateral behaviour of rock was rendered through specific parameters that modelled the extremes of full stiffness recovery or no stiffness recovery during load reversal. This model, despite its simplicity, captures the significant features, including correct failure modes and average stress–strain responses, of heterogeneous rock under uniaxial tension and compression tests, as shown in the simulations results.

The electric field and the consequent power density distribution in the test rock sample due to microwave irradiation, solved in COMSOL software, became the input load in the developed staggered explicit scheme to simulate the thermo-mechanical problem. The temperature rise and the consequent thermally induced damage were successfully estimated in the numerical simulations. The electric field distribution was qualitatively and quantitatively in line with previous numerical studies. The maximum reduction in compressive strength, after performing mechanical tests on previously irradiated numerical samples,

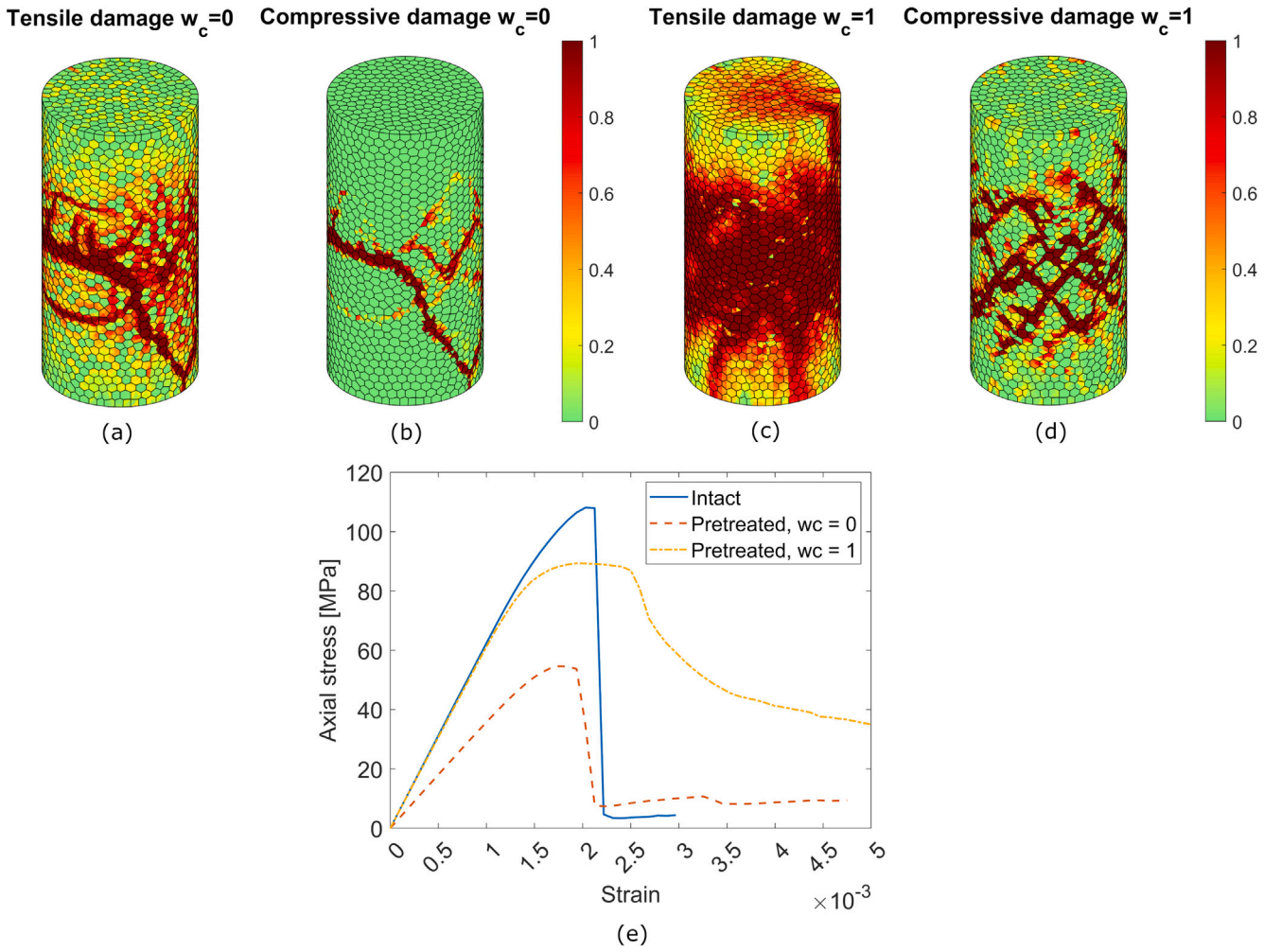

Fig. 12. Simulation results for microwave pretreated sample (Mesostructure 1). Failure modes represented as distributions of damage variables with $w_t = 0$ and $w_c = 0$ (a)–(b) and with $w_t = 0$ and $w_c = 1$ (c)–(d) during uniaxial compression on pretreated samples. Corresponding axial stress–strain curves (e).

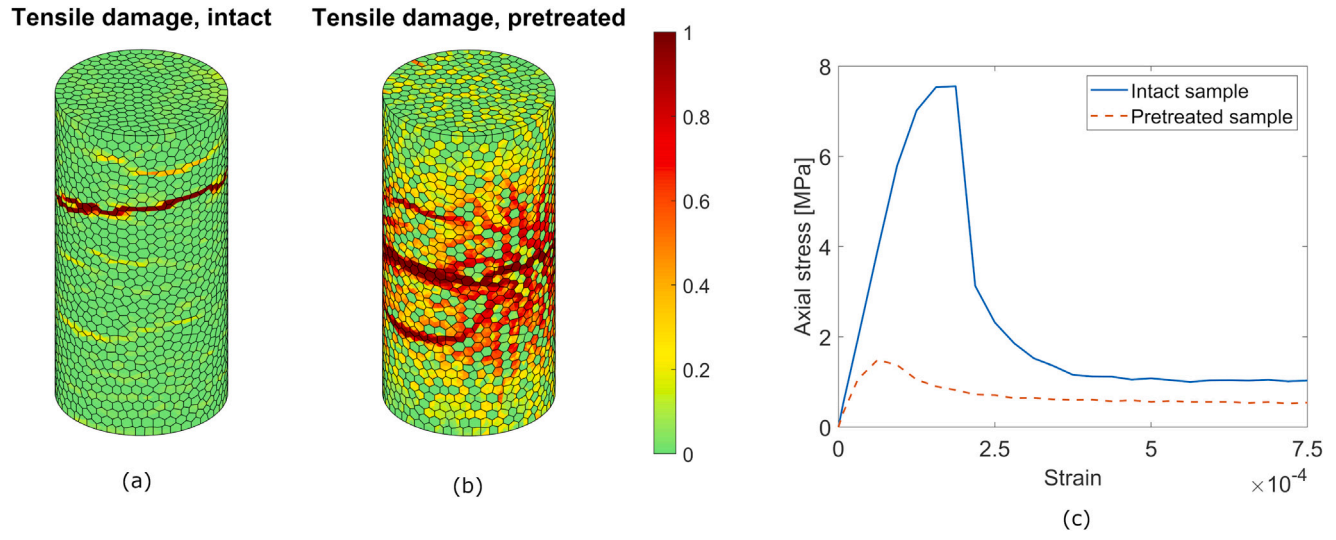

Fig. 13. Simulation results for tension test on microwave pretreated samples (Mesostructure 1). Failure modes represented as distributions of damage variables for intact (a) and pretreated specimen (b). Axial stress–strain curves for intact and pretreated specimen (c).

was 18 % if no elastic stiffness was recovered and 48 % if full elastic stiffness was gained again. These values may be considered a feasible lower and upper limit of the real case.

These very positive figures are influenced by the long heating times (60 s) and strategic positioning of the sample in the oven. A further development should incorporate modelling of intergranular cracks at mineral boundaries to replicate the experimental results of previous studies. Finally, in order to fully evaluate the weakening effect of microwave heating pretreatment on compressive strength of rock, the present model should be validated by ad hoc experiments.

CRediT authorship contribution statement

Martina Pressacco: Conceptualization, Methodology, Software, Writing – original draft, Writing – review & editing, Visualization, Funding acquisition. **Jari J.J. Kangas:** Conceptualization, Methodology, Software, Writing – review & editing. **Timo Saksala:** Conceptualization, Methodology, Software, Writing – review & editing, Supervision.

Declaration of competing interest

The authors declare the following financial interests/personal relationships which may be considered as potential competing interests: Martina Pressacco reports financial support was provided by K H Renlund Foundation.

Data availability

The data that has been used is confidential.

Acknowledgement

The work of M. Pressacco is supported by a grant of K.H. Renlund Foundation, Finland.

References

Ali, A., Bradshaw, S., 2009. Quantifying damage around grain boundaries in microwave treated ores. Chem. Eng. Process.: Process Intensif. 48 (11), 1566–1573.
Ali, A., Bradshaw, S., 2010. Bonded-particle modelling of microwave-induced damage in ore particles. Miner. Eng. 23 (10), 780–790.
Basu, A., Mishra, D., Roychowdhury, K., 2013. Rock failure modes under uniaxial compression, Brazilian, and point load tests. Bull. Eng. Geol. Environ. 72, 457–475.
Batchelor, A., Jones, D., Plint, S., Kingman, S., 2015. Deriving the ideal ore texture for microwave treatment of metalliferous ores. Miner. Eng. 84, 116–129.
Cemhan, S., Kelly, G., Schmitt, J., 2019. The effect of microwave irradiation on hard rock as pre-treatment to increase the efficiency of underground mining. In: CERC 2019.
Chen, T.T., Dutrizac, J.E., Haque, K.E., Wyslouzil, W., Kashyap, S., 1984. The relative transparency of minerals to microwave radiation. Can. Metall. Quart. 23 (3), 349–351.
Chen, T., Xiong, W., Cui, G., Yu, H., Elsworth, D., Shi, B., Feng, X., Pan, Z., 2021. An effective dual-medium approach to simulate microwave heating in strongly heterogeneous rocks. Geomech. Geophys. Geo-energ. Geo-resour. 17 (101).
Clauser, C., Huenges, E., 2013. Thermal conductivity of rocks and minerals. In: Ahrens, T.J. (Ed.), Rock Physics & Phase Relations. American Geophysical Union (AGU), pp. 105–126.
Denoual, C., Hild, F., 2000. A damage model for the dynamic fragmentation of brittle solids. Comput. Method. App. M 183 (3), 247–258.
Eberhardt, E., Stead, D., Stimpson, B., 1999. Quantifying progressive pre-peak brittle fracture damage in rock during uniaxial compression. Int. J. Rock Mech. Min. 36 (3), 361–380.
Felippa, C.A., Park, C.K., 1980. Staggered transient analysis procedures for coupled mechanical systems: Formulation. Comput. Method. Appl. M 24 (1), 61–111.
Gao, M.Z., Yang, B.G., Xie, J., Ye, S.Q., Liu, J.J., Liu, Y.T., Tang, R.F., Hao, H.C., Wang, X., Wen, X.Y., Zhou, X.M., 2022. The mechanism of microwave rock breaking and its potential application to rock-breaking technology in drilling. Pet. Sci..
Ge, Z., Sun, Q., Xue, L., Yang, T., 2021. The influence of microwave treatment on the mode I fracture toughness of granite. Eng. Fract. Mech. 249, 107768.
Grassl, P., Jirásek, M., 2006. Damage-plastic model for concrete failure. Int. J. Solids Struct. 43 (22), 7166–7196.
Hahn, G.D., 1991. A modified Euler method for dynamic analyses. Internat. J. Numer. Methods Engrg. 32 (5), 943–955.
Hao, J., Li, Q., Qiao, N., 2020. Effects of microwave irradiation on impact comminution and energy absorption of magnetite ore. In: Proceedings of China Rock 2020. In: IOP Conference Series: Earth and Environmental Science, China Rock 2020 23-26 October 2020, Beijing, China, vol. 570, IOP Publishing Ltd, Bristol, UK.
Hartlieb, P., 2013. Investigations on the Effects of Microwaves on Hard Rocks (Ph.D. thesis). Montanuniversität Leoben, Leoben, Austria.
Hartlieb, P., Toifl, M., Kuchar, F., Meisels, R., Antretter, T., 2016. Thermo-physical properties of selected hard rocks and their relation to microwave-assisted comminution. Miner. Eng. 91, 34–41.
Hassani, F., Nekoovaght, P.M., Radziszewski, P., Waters, K.E., 2011. Microwave Assisted Mechanical Rock Breaking. In: Proceedings of 12th ISRM Congress, International Society for Rock Mechanics and Rock Engineering, Beijing, China.
Haus, H.A., Melcher, J.R., 1989. Electromagnetic Fields and Energy. Prentice-Hall, Englewood Cliffs, NJ.
Homand-Etienne, F., Houpert, R., 1989. Thermally induced microcracking in granites: characterization and analysis. Int. J. Rock Mech. Min. 26 (2), 125–134.
Inserra, C., Biwa, S., Chen, Y., 2013. Influence of thermal damage on linear and nonlinear acoustic properties of granite. Int. J. Rock Mech. Min. 62, 96–104.
Jackson, J.D., 1998. Classical Electrodynamics. John Wiley & Sons; New York.
Jaeger, J.C., Cook, N.G.W., Zimmermann, R., 2007. Fundamentals of Rock Mechanics. Wiley-Blackwell, Malden, USA, p. 488.
Jeswiet, J., Szekeres, A., 2016. Energy consumption in mining comminution. Procedia CIRP 48, 140–145, The 23rd CIRP Conference on Life Cycle Engineering.
Jones, D.A., Kingman, S.W., Whittles, D.N., Lowndes, I.S., 2005. Understanding microwave assisted breakage. Miner. Eng. 18 (7), 659–669.
Jones, D.A., Kingman, S.W., Whittles, D.N., Lowndes, I.S., 2007. The influence of microwave energy delivery method on strength reduction in ore samples. Chem. Eng. Process. 46 (4), 291–299.
Ju, Y., Zhu, Y., Zhou, H., Ge, S., Xie, H., 2021. Microwave pyrolysis and its applications to the in situ recovery and conversion of oil from tar-rich coal: An overview on fundamentals, methods, and challenges. Energy Rep. 7, 523–536.
Kahraman, S., Canpolat, A.N., Fener, M., 2020. The influence of microwave treatment on the compressive and tensile strength of igneous rocks. Int. J. Rock Mech. Min. 129, 104303.
Kingman, S., Rowson, N., 1998. Microwave treatment of minerals-A review. Miner. Eng. 11 (11), 1081–1087.
Lee, J., Fenves, G.L., 1998. Plastic-damage model for cyclic loading of concrete structures. J. Eng. Mech. 124 (8), 892–900.
Li, J., Kaunda, R.B., Arora, S., Hartlieb, P., Nelson, P.P., 2019. Fully-coupled simulations of thermally-induced cracking in pegmatite due to microwave irradiation. J. Rock Mech. Geotech. Eng. 11 (2), 242–250.
Lubliner, J., Oliver, J., Oñate, E., 1989. A plastic-damage model for concrete. Int. J. Solids Struct. 25 (3), 299–326.
Ma, Z., Zheng, Y., Sun, T., Li, J., 2021. Thermal stresses and temperature distribution of granite under microwave treatment. In: Proceedings of 11th Conference of Asian Rock Mechanics Society 21-25 October 2021. In: IOP Conf. Ser.: Earth Environ. Sci, vol. 861, (032094), IOP Publishing Ltd, Bristol, UK.
Mardalizad, A., Scazzosi, R., Manes, A., Giglio, M., 2018. Testing and numerical simulation of a medium strength rock material under unconfined compression loading. J. Rock Mech. Geotech. Eng. 10 (2), 197–211.
Martins, J.M.P., Neto, D.M., Alves, J.L., Oliveira, M.C., Laurent, H., Andrade-Campos, A., Menezes, L.F., 2017. A new staggered algorithm for thermomechanical coupled problems. Int. J. Solids Struct. 122–123, 42–58.
McGill, S.L., Walkiewicz, J.W., Smyres, G.A., 1988. The effects of power level on the microwave heating of selected chemicals and minerals. MRS Proc. 124, 247.
Mehdizadeh, M., 2015. Microwave/RF Applicators and Probes - For Material Heating, Sensing, and Plasma Generation. Elsevier, London, Uk.
Molaro, J.L., Byrne, S., Langer, S.A., 2015. Grain-scale thermoelastic stresses and spatiotemporal temperature gradients on airless bodies, implications for rock breakdown. J. Geophys. Res. Planet 120 (2), 255–277.
Monk, P., 2003. Finite Element Methods for Maxwell's Equations. Oxford University Press, Oxford, UK.
Ngo, M., Brancherie, D., Ibrahimbegovic, A., 2014. Softening behavior of quasi-brittle material under full thermo-mechanical coupling condition: Theoretical formulation and finite element implementation. Comput. Method Appl. M 281, 1–28.
Nicco, M., Holley, E.A., Hartlieb, P., 2020. Textural and mineralogical controls on microwave-induced cracking in granites. Rock Mech. Rock Eng. 53, 4745—4765.
Ottosen, N.S., Ristinmaa, M., 2005. The Mechanics of Constitutive Modeling. Elsevier Science Ltd, Oxford, pp. 637–672.
Peinsitt, T., Kuchar, F., Hartlieb, P., Moser, P., Kargl, H., Restner, U., Sifferlinger, N., 2010. Microwave heating of dry and water saturated basalt, granite and sandstone. Int. J. Min. Eng. 2 (1), 18–29.
Poole, C., Darwazeh, I., 2016. Microwave Active Circuit Analysis and Design. Academic Press, Oxford, UK.
Pozar, D.M., 2011. Microwave Engineering. Wiley, Hoboken, NJ.

Pressacco, M., Kangas, J., Saksala, T., 2022. Numerical modelling of microwave heating assisted rock fracture. Rock Mech. Rock Eng. 55, 481–503.
Pressacco, M., Saksala, T., 2020. Numerical modelling of heat shock-assisted rock fracture. Int. J. Numer. Anal. Methods 44 (1), 40–68.
Quey, R., Dawson, P., Barbe, F., 2011. Large-scale 3D random polycrystals for the finite element method: Generation, meshing and remeshing. Comput. Methods Appl. Mech. Engrg. 200, 1729—1745.
Saksala, T., 2010. Damage–viscoplastic consistency model with a parabolic cap for rocks with brittle and ductile behavior under low-velocity impact loading. Int. J. Numer. Anal. Methods 34 (13), 1362–1386.
Saksala, T., Pressacco, M., Holopainen, S., Kouhia, R., 2019. Numerical modelling of heat generation during shear band formation in rock. Rakenteiden mekaniikka 52.
Santos, T.C., Costa, L.C., Valente, M.A., Monteiro, J., Sousa, J., Santos, T., 2010. 3D electromagnetic field simulation in microwave ovens: a tool to control thermal runaway. In: Proceedings of COMSOL Conference. Paris, France.
Schön, J., 2011. Physical Properties of Rocks. Elsevier Science and Technology, United Kingdom.
Shadi, A., Ahmadihosseini, A., Rabiei, M., Samea, P., Hassani, F., Sasmito, A.P., Ghoreishi-Madiseh, S.A., 2022. Numerical and experimental analysis of fully coupled electromagnetic and thermal phenomena in microwave heating of rocks. Miner. Eng. 178, 107406.
Tang, C., Hudson, J., 2010. Rock Failure Mechanisms: Illustrated and Explained. CRC Press, London, UK, p. 364.
Toifl, M., Hartlieb, P., Meisels, R., Antretter, T., Kuchar, F., 2017. Numerical study of the influence of irradiation parameters on the microwave-induced stresses in granite. Miner. Eng. 103–104, 78–92.
Toifl, M., Meisels, R., Hartlieb, P., Kuchar, F., Antretter, T., 2016. 3D numerical study on microwave induced stresses in inhomogeneous hard rocks. Miner. Eng. 90, 29–42.
Vázquez, P., Shushakova, V., Gómez-Heras, M., 2015. Influence of mineralogy on granite decay induced by temperature increase: Experimental observations and stress simulation. Eng. Geol. 189, 58–67.
Vosteen, H.D., 2003. Influence of temperature on thermal conductivity, thermal capacity and thermal diffusivity for different types of rock. Phys. Chem. Earth PT A,B,C 28 (9), 499–509, Heat Flow and the Structure of the Lithosphere.
Wang, W.M., 1997. Stationary and Propagative Instabilities in Metals - A Computational Point of View (Ph.D. thesis). Delft University of Technology, Delft, Netherlands.
Wang, F., Konietzky, H., 2019. Thermo-mechanical properties of granite at elevated temperatures and numerical simulation of thermal cracking. Rock Mech. Rock Eng. 52, 3737—3755.
Wang, G., Radziszewski, P., Ouellet, J., 2008. Particle modeling simulation of thermal effects on ore breakage. Comput. Mater. Sci. 43 (4), 892–901.
Wang, H., Rezaee, M., Saeedi, A., Josh, M., 2017. Numerical modelling of microwave heating treatment for tight gas sand reservoirs. J. Pet. Sci. Eng. 152, 495–504.
Wang, W.M., Sluys, L.J., de Borst, R., 1997. Viscoplasticity for instabilities due to strain softening and strain-rate softening. Internat. J. Numer. Methods Engrg. 40 (20), 3839–3864.
Waples, D.W., Waples, J.S., 2004. A review and evaluation of specific heat capacities of rocks, minerals, and subsurface fluids. Part 1: Minerals and nonporous rocks. Nat. Resour. Res. (13), 97–122.
Wei, W., Shao, Z., Chen, W., Qiao, R., Yuan, Y., Cheng, J., 2021. Heating process and damage evolution of microwave absorption and transparency materials under microwave irradiation. Geomech. Geophys. Geo-energ. Geo-resour. 7 (86).
Whittles, D., Kingman, S., Reddish, D., 2003. Application of numerical modelling for prediction of the influence of power density on microwave-assisted breakage. Int. J. Miner. Process. 68 (1), 71–91.
Xu, T., Yuan, Y., Heap, M.J., Zhou, G.L., Perera, M., Ranjith, P., 2021. Microwave-assisted damage and fracturing of hard rocks and its implications for effective mineral resources recovery. Miner. Eng. 160, 106663.
Zhang, Q.B., Zhao, J., 2014. A review of dynamic experimental techniques and mechanical behaviour of rock materials. Rock Mech. Rock Eng. 47 (4), 1411–1478.
Zheng, Y.L., Zhao, X.B., Zhao, Q.H., Li, J.C., Zhang, Q.B., 2020. Dielectric properties of hard rock minerals and implications for microwave-assisted rock fracturing. Geomech. Geophys. Geo-Energy Geo-Resour. 6.